15th EAWE PhD Seminar on Wind Energy
29–31 October 2019
Centrale Nantes, France

An LES characterization of turbulent and wave induced flows in the atmospheric boundary layer above regular non-linear swells.

Liad Paskin, Boris Conan, Yves Perignon, and Sandrine Aubrun

École Centrale de Nantes

E-mail: liad.paskin@ec-nantes.fr

Abstract

Actually on coastal areas, the wind energy industry migrates to the offshore environment, where huge spaces are still available in stronger and better behaved wind conditions. The concerned flow is hold by a turbulent atmospheric boundary layer (ABL) where the ocean's dynamics might significantly alter the atmospheric flow through higher heat capacity and complex wind-wave interactions important in fairly common situations. Besides the departure of the ABL from onshore predictions, other important phenomena result from wind-wave interactions, creating specific (maybe extreme) sea state conditions and impacting global atmospheric and ocean circulations.

The ABL is mostly disturbed on a limited region referred as the wave boundary layer (WBL). Focusing in the WBL generated by non-equilibrium old-seas conditions, the free-surface position and velocities are here prescribed into a Large Eddy Simulation (LES) according to a fifth order Stokes solution. The swell disturbances on the WBL are explored through mean profiles and spectral analyses. An original non-linear definition of a wave induced flow is presented, considering correlated turbulent and wave induced motions thus accessing the coupled dynamics between those fields and inducing a natural precise definition of the WBL height. A robust definition of the wave induced flow and its coupling with turbulent dynamics would possibly allow its modeling in low-fidelity numerical models. Employing the proposed decomposition, the turbulent flow characteristics are recovered as expected in a flat bottom ABL, though some of its scales change considerably forced by the WBL below.

Keywords: Offshore wind farm; Ocean Engineering; Marine atmospheric boundary layer; Large eddy simulation.

1 Introduction

This work continues the development presented in [1], where a fully deterministic numerical model is applied coupling air and water domains' resolutions. Through the Large Eddy Simulation (LES) presented in [2] a fully turbulent and incompressible fluid describes the atmosphere, assuming negligible molecular viscosity and the Boussinesq approximation for compressibility. A high order spectral (HOS) method developed in ECN ([3]) solves the fully non-linear potential waves equations, discretized on the free-surface. One way coupling is achieved imposing the free-surface position and velocity field from HOS into the atmosphere and have been studied by [1], who also introduced a two-way coupling: forcing the HOS with the atmospheric induced pressure. Though further works shall access and improve the coupled solver capabilities, current objectives allow the coupling and wave field solving to be here neglected. A more fundamental approach is so adopted to discuss: (i) the definition of a wave induced flow in the ABL; (ii) the characterization of the WBL within its wave induced and turbulent motions; and (iii) the impact of the WBL in the flow above. This introduction extends into governing equations and numerical strategy descriptions in sections 1.1 and 1.2; the impact of the WBL in the atmospheric flow is globally accessed through mean velocity and turbulent profiles in 2.1 and the WBL definition proposed in section 2.2 being characterized by spectral analyses and relative intensity compared to turbulence.

The Monin-Obukhov (MO) similarity theory ([4]), has been shown a successful model to describe mean wind turbulent profiles in non-neutral (specially convective, day time) conditions over static rough

surfaces. It is observed though, that the mean wind profile considerably deviates from MO predictions within the WBL. Theory agrees to observation (c.f. [5], [6]) that the wave induced disturbances extends into limited regions above the free surface. Though coupled to this inner layer, the outer flow behaves similarly to static atmospheric flows such as usually described by the MO theory. Definitions of the inner layer's height are not unique as discussed in [6].

When a swell encounters a weak aligned wind, the momentum transfer occurs from the sea into the atmosphere in a situation referred as old seas, oposed to the wave growing phase referred as young seas. The momentum transfer is observed to be correlated to the deviations from MO theory, and become important in young and old seas. Current work will focus on the canonical case where a swell labeled by its phase velocity c encounters light wind conditions with initial wall friction τ_w, specific mass ρ and mean friction velocity $\overline{u^*} = \sqrt{\overline{\tau}_w/\rho}$. Such case is characterized by high wave ages $WA = c/\overline{u^*}$ and strong disturbances in the wind field, as the WBL extension is somehow proportional to the wave's length. Being the swell evolving time scale much larger than the ABL's, it is expected that geostrophic forcing conditions would rapidly change before the waves' dynamics adapt to the wind field above, so that the wave field is here prescribed through the 5th order Stokes solution given in [7].

In a simplified framework, this scenario has been subject to numerous theoretical studies describing the wave growth phenomena, as one should note the pioneer works of [8], [9], [10], [11], [12], [13] and [14]. Multiple field measuring campaigns are nowadays available forming the basis to comprehensive conclusions about the marine ABL, such as: FINO1 explored and described in [15] and [16]; ASIT in [16]; CBLAST and others in [17]. The development of numerical tools is essential for prediction purposes and has been extensively employed, e.g., by atmospheric forecast systems such as the ECMWF, improved in its marine ABL model by [18]. Global atmospheric models are forced to use, at their finest, grid resolutions of tens of kilometers, requiring high level of modeling including the momentum transfer with the WBL. Focusing in parameterizing the wave effect on the the upper part of the ABL where MO is expected to hold, Charnock's parametrization [19] is followed by many, s.a. reviewed and extended by [20], [17], [15] and [16].

At local scales applications, such as wind farms or urban forecast and pollutant dispersion, one is allowed and required to reduce the modeling level. Modelling turbulence effects in the average flow, (Unsteady) RANS one or two equation closures are yet the most applied type of numerical model into CFD simulations of ABL flows at local scales ([21], [22]). Fully resolved turbulence is achievable through Direct Numerical Simulations (DNS) with limited Reynolds numbers, and has been employed, e.g. in [23]: Later developed into a Large Eddy Simulation (LES) model ([24], [2]), which is here employed to resolve the ABL flow. The LES approach introduces limited level of modeling into the isotropic, smallest turbulent scales, theoretically resolving most of the turbulent energy and specially the anisotropic motions determined by the problem's boundary conditions: It is a methodology now responsible for modeling numerous atmospheric studies, regarding different phenomena and discretization scales (dx) ranging, e.g., from climate ($dx \sim O[\ km]$) to local wind farming ($dx \sim O[\ m]$) scales ([25], [26]).

1.1 Governing equations

Coriolis forces are neglected. An incompressible fluid is considered with the Boussinesq approximation for compressibility (c.f. [27]) acting in the buoyant terms of momentum and turbulent equations. Molecular viscosity is neglected in the fully turbulent flow. The balance equations are filtered according to an LES approach: Let $\boldsymbol{u}(\boldsymbol{x},t) = (u,v,w)$ and $p(\boldsymbol{x},t)$ be the spatially filtered velocity and pressure fields; $\boldsymbol{u}^{SGS}$ and p^{SGS} the residual fields; $p^* = p + (2e/3)$ the modified pressure accounting for the residual turbulent kinetic energy ($e = u_i^{SGS}u_i^{SGS}/2$) effect; $\rho(\boldsymbol{x},t) = -\rho_\infty(\theta-\theta_\infty)/\theta_\infty$ the specific mass dependent on the virtual temperature θ and the reference values $[p_\infty, \theta_\infty]$; $\boldsymbol{S} = \left[\nabla\boldsymbol{u} + (\nabla\boldsymbol{u})^T\right]/2$ the strain rate tensor; $\boldsymbol{\tau}^{SGS} = -2\nu_t\boldsymbol{S}$ the sub-grid-scale modeled shear stress tensor defined within the eddy viscosity hypothesis scope and dependent on the turbulent viscosity ν_t; g the gravitational acceleration; the mass and momentum balances are written as equations 1, and the residual turbulent kinetic energy solved by the Deardorff single equation turbulence model as in equation 2:

$$\frac{\partial u_j}{\partial x_j} = 0, \qquad \frac{\partial u_i}{\partial t} + \frac{\partial (u_j u_i)}{\partial x_j} = -\frac{1}{\rho_\infty}\frac{\partial p}{\partial x_i} - \frac{\partial \tau_{ij}^{SGS}}{\partial x_j} - \frac{\rho}{\rho_\infty} g\delta_{i3}, \text{and} \tag{1}$$

$$\frac{\partial e}{\partial t} + \frac{\partial (u_i e)}{\partial x_i} = (2\nu_t S_{ij}) S_{ij} - \frac{g}{\theta_\infty} \nu_h \frac{\partial \theta}{\partial x_3} + \frac{\partial}{\partial x_j} \left(2\nu_t \frac{\partial e}{\partial x_j} \right) - \epsilon. \tag{2}$$

The turbulent dissipation $\epsilon = c_\epsilon e^{3/2}/\Delta_f$ is determined according to the filter length scale $\Delta_f = [(3/2)^2 \Delta x_1 \Delta x_2 \Delta x_3]^{1/3}$. The turbulent kinematic viscosity and diffusivity are respectively $\nu_t = c_k l e^{1/2}$ and $\nu_h = (1 + 2l/\Delta_f)\nu_t$, where l is usually equal to Δ_f, but is reduced above an inversion layer characteristic to stable stratification regimes. The governing equations are transformed from the deformed moving grid into the cartesian numerical space and the full set of equations presented with the constants values, e.g., in [24].

1.2 Numerical strategy

The governing equations are solved in a moving grid by the pseudo-spectral numerical method given in [24]. The physical space $(x_1, x_2, x_3) = (x, y, z)$ is mapped into the computational space $(\xi = x, \eta = y, \zeta = \zeta(x, y, t))$. The pseudo-spectral discretization applies to (ξ, η) directions and a second order finite difference to ζ direction. The third-order Runge-Kutta time-stepping scheme is employed with fixed time step 0.0595 s. A uniform pressure gradient is imposed in x direction driving the flow so that in flat bottom terrains the stresses' integral balance in the boundaries gives mean friction velocity $\overline{u^*} = 0.21$ m/s. For the neutral stability considered the difference between the first cell and surface tangential and normal velocities $(\Delta u_{[\xi,\eta]}, \Delta u_\zeta)$ are given by a log-law type boundary condition (BC): $\Delta u_{[\xi,\eta]} = (u^*_{[\xi,\eta]})/\kappa) \ln(z/z_0)$ and $\Delta u_\zeta = 0$ with roughness length $z_0 = 10^{-4}$ m and von Karman constant $\kappa = 0.4$. The friction velocity $u^*_{[\xi,\eta]}$ is obtained point-wise from turbulent resolved and modeled stresses. Residual turbulent kinetic energy flux in the surface and all fluxes in the upper boundary are null, except for the vertical velocities which are null instead of their fluxes as a no penetration condition in the upper boundary. Symmetry BCs naturally follow from the pseudo-spectral approach in (ξ, η) directions.

Two cases are presented: Case 01 is the reference considering a flat terrain, while case 02 introduce the moving terrain here described. The free-surface position and velocities are prescribed according to the fifth order Stokes solution given in [7]. The regular wave propagates with length $\lambda = 2\pi/k = 100$ m, amplitude $a = 3.18$ m ($ka = 0.2$), and in infinite depth so that the phase velocity obtained through the dispersion equation is $c = 12.7$ m/s. With the reference friction velocity $\overline{u^*} = 0.21$ m/s case 02 presents WA $= c/\overline{u^*} = 60$. The considered domain has size $(4, 2, 5)\lambda$ and is discretized with $(512, 256, 94)$ cells in (x, y, z) directions respectively. The cells are equally distributed in (x, y) but not in z where it grows according to an algebraic mapping: The first grid size in z direction is 0.2604 m and it grows with a constant ratio of 1.05.

Originally the flow field is constructed from mean theoretical solution for flat plate turbulent boundary layers superposed to artifical, ramdomly generated turbulent motions. The initialization procedure then considers the buoyant effects on the momentum equations to generate resolved turbulence as further initial solution and have been previously studied for the present grid and friction velocity in [1]. The results here presented follow from a converged restart after buoyant terms are set back to zero representing neutral stratification. The wave forcing in the lower BC linearly evolves from null till its 5th order solution during 120 s.

2 Results and discussion

2.1 Mean Profiles

A spatial average, denoted by $(\cdot^{[\xi,\eta]})$, is applied through each (ξ, η) horizontal computational plane and followed by a time average through the period t_{avg} for the quantities presented in this section, with the total average operator denoted by $(\bar{\cdot})$. Fluctuations $(\cdot')$ are obtained deducing filtered fields from their spatial averages so that $\boldsymbol{u} = \overline{\boldsymbol{u}}^{[\xi,\eta]} + \boldsymbol{u}'$. The friction velocity $u^*_{[\xi,\eta]} = (\tau^w_{[\xi,\eta]}/\rho)^{1/2}$ is obtained in the first grid cell summing resolved and modeled turbulent shear stresses $\tau^w_i = u'_i u'_j (1 - \delta_{ij}) + \tau^{SGS}_{ij} \delta_{jj}$ and its averaged history $\overline{u^*} = \overline{||\boldsymbol{u}^*||}$ presented in figure 1a considering $t_{avg} = [0.1; 1]$ hr for each test case. The introduction of a prescribed swell suddenly decreases the friction velocity at the surface: An effect which is reduced as the wind field adapts to the bottom BC with time, though remaining about 10% lower than the reference case. Turbulent fluctuations are still noticed when $t_{avg} = 0.1$ hr, but are mostly filtered

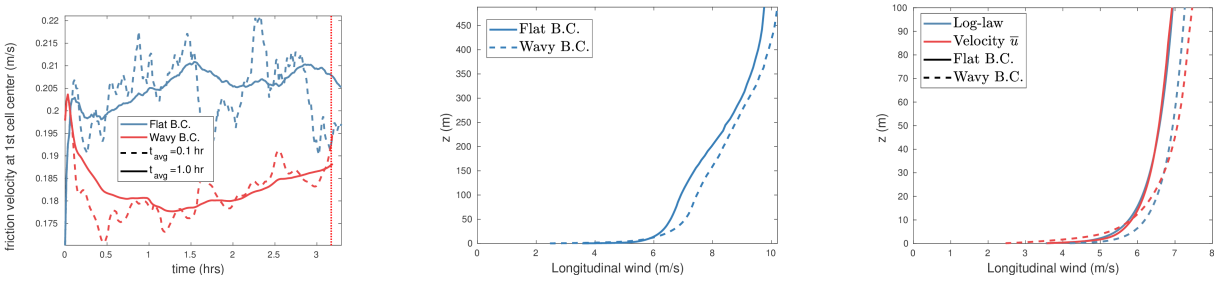

(a) Mean friction velocity. (b) Mean velocity. (c) Mean velocity and log-law fit.

Figure 1: Friction velocity history and mean velocity profiles.

Case	RMS diff (m/s)	$C_d(\kappa = 0.41)$	$\kappa(C_d = 1)$	$z_0(m)$
Flat BC	0.07	0.99	0.41	$1.2 \cdot 10^{-4}$
Wavy BC	0.33	1.04	0.39	$1.7 \cdot 10^{-5}$

Table 1: Log-law fitting to longitudinal velocities within $z < 100$ m, shown in figure 1c.

out when $t_{avg} = 1$ hr. The quantities further explored through this section are averaged with $t_{avg} = 1$ hr and probed during the final time steps, denoted by the vertical red dashed line in figure 1a.

The mean wind fields are averaged with $t_{avg} = 1$ hr and shown in figures 1b and 1c for $z \leq 500m$ and $z \leq 100m$ respectively. Related to the initialization procedure as observed in all cases, statistics have nicely converged for $z \leq 100m$, but not above where the velocity profiles strongly deviate from the expected log-law behavior in figure 1b. A log-law profile $\overline{u}_1 = (C_d u^*/\kappa)\ln(z/z_o)$ with parameters C_d/κ and z_0 is fitted minimizing the RMS difference for the obtained u^* and $z \leq 100m$. The log-law profile is superposed to the obtained velocity profile in 1c and the obtained parameters shown in table 1: The introduction of waves multiply the RMS difference between resolved and fitted profiles by a factor of ~ 5; the friction velocity (fig. 1a) decreases $\sim 10\%$ but the factor C_d/κ increases $\sim 10\%$ so that the apparent friction velocity $C_d u^*/\kappa$ change is very small ($\sim 0.3\%$); the roughness length decreases by a factor of ~ 7; the control case 01 closely reproduce the theoretical values for a neutral flat bottom ABL with the imposed BC, i.e., $u^* = 0.21$; $C_d = 1$; $\kappa = 0.4$; $z_0 = 10^{-4}m$.

Mean turbulent profiles are exemplified in figure 2. The turbulent kinetic energy (tke) resolved ($0.5\overline{u_i' u_i'}$) and modeled ($\overline{e}$) parts are shown in figure 2a: Through the introduction of waves the tke is greatly increased on the wave's vicinity, trending to non-disturbed values when $z \sim 20$. Main source of momentum flux along z, resolved ($0.5\overline{u'w'}$) and modeled (τ_{13}^{SGS}) cross-correlations are exposed in figure 2b: The total flux is considerably increased up to $z > 100m$. As the total flux is reduced in magnitude, so is the equivalent turbulent kinematic viscosity $\nu_t = -(\tau_{13}^{SGS} + 0.5\overline{u'w'})/(2S_{13})$ averaged profiles with respect to non-disturbed values in figure 2c. The profiles' slope resembles its non-disturbed values sooner than the values itself, as one might here speculate the fluctuations behave expected in classical shear flows' turbulence, further forced by the WBL below.

2.2 Wave induced flow

For a deterministic assessment of the wave induced perturbations, it is useful to consider a triple decomposition, where the velocity and pressure fields decompose respectively into $\boldsymbol{u} = \overline{\boldsymbol{u}} + \boldsymbol{u'} + \tilde{\boldsymbol{u}}$ and $p = \overline{p} + p' + \tilde{p}$, being $[\boldsymbol{u'}, p']$ and $[\tilde{\boldsymbol{u}}, \tilde{p}]$ the turbulent and wave related flows. Imposing a filter to retain the wave coherent flow ($\phi = \overline{\phi} + \tilde{\phi}^C + \phi'^C$) that neglects its correlation with turbulence, [28] presents dynamic equations for the the decomposed fields uncoupled between wave coherent ($\tilde{\phi}^C$) and turbulent (ϕ'^C) motions. This methodology led to fruitful conclusions about the WBL, e.g. in [28] and [29] that define the filter projecting a time signal $[\boldsymbol{u}(t), p(t)]$ into the vector space of all wave coherent signals, i.e., those occurring at the same frequencies as the wave profile $\eta(t)$. Alternatively we employ the wave coherent filter (Eq. 3) in space. Let $\hat{\eta}_k(x)$ be the in-quadrature counterpart of the k^{th} wave number free surface elevation $\eta_k(x)$ so that:

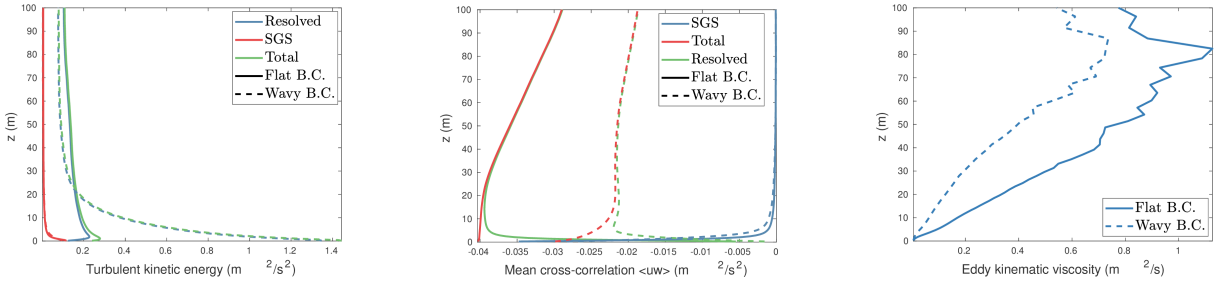

(a) Turbulent kinetic energy (b) Mean cross correlation $\overline{u'w'}$ (c) Eddy kinematic viscosity

Figure 2: Mean turbulent profiles.

$$\tilde{\boldsymbol{u}}^{C}(\boldsymbol{x},t) = \sum_k \left(\frac{\overline{\boldsymbol{u}(\boldsymbol{x},t)\eta_k(x,t)}^{[x]}}{||\eta_k||^2}\eta_k(x,t) + \frac{\overline{\boldsymbol{u}(\boldsymbol{x},t)\hat{\eta}_k(x,t)}^{[x]}}{||\hat{\eta}_k||^2}\hat{\eta}_k(x,t) \right), \tag{3}$$

effectively filters flow motions occurring with length scale $2\pi/k$, where $\overline{\cdot}^{[x]}$ and $||\cdot||$ indicate average and norm in x direction. Considering the triple decomposition as in equation 3 filters not only wave-induced, but also turbulent motions which occur in the waves' lengths, leading to non-physical drops in the turbulent spectra (figure 3b). A non-linear modification is then proposed to the wave coherent (WC) filter 3, thus renamed wave induced (WI) filter in eq. 4 such that $\phi = \overline{\phi} + \tilde{\phi}^{I} + \phi'^{I}$. Let $0 \leq f_{ki}^2(z) \leq 1$ be the fraction of wave induced energy ($\tilde{E}_{ii}^I(k) = 0.5\tilde{u}_i^I\tilde{u}_i^I$) in the total fluctuations' kinetic energy ($E_{ii}(k) = 0.5[u_i - \overline{u_i}][u_i - \overline{u_i}]$) contained in the wave number k and velocity component i, the wave induced flow is:

$$\tilde{\boldsymbol{u}}^{I}(\boldsymbol{x},t) = \boldsymbol{f}_k(z) \cdot \sum_k \left(\frac{\overline{\boldsymbol{u}(\boldsymbol{x},t)\eta_k(x,t)}^{[x]}}{||\eta_k||^2}\eta_k(x,t) + \frac{\overline{\boldsymbol{u}(\boldsymbol{x},t)\hat{\eta}_k(x,t)}^{[x]}}{||\hat{\eta}_k||^2}\hat{\eta}_k(x,t) \right), \tag{4}$$

where f should be determined considering turbulent and wave coherent flow specific characteristics, here based on the turbulent spectra. An optimization, gradient descent algorithm is implemented to obtain the value of f that minimizes the second derivative of turbulent velocities and pressure spectra in the wave filtered lengths scales. It is worth noting that these definitions of wave coherent and induced flows are suitable for swell conditions with discrete wave spectrum: The proposed methodology is not expected to work if the wave spectrum is continuous instead. Nevertheless, it is possible that a parametrization of f based on discrete wave spectras would enable to the modelling of f in continuous distributed cases. Identifying the waves' signature for example through space-time spectra such as presented in [30] would possibly allow a more general definition of f through the introduction of considerable computational effort.

The filter proposed in equation 3 assumes wave coherent and turbulent motions are not correlated ($[\tilde{\cdot}]' = 0$): A convenient property that allows the uncoupled form of their balance equations presented in [28], but which is lost with equation 4. It appears that wave induced and turbulent correlations are a key point into understanding the WBL behavior and the disturbance in turbulent motions: It is through these coupled dynamics' that turbulent scales are distorted as wave induced motions merge into the turbulent cascade along the WBL.

The general one dimensional correlation function of two variables ϕ_1 and ϕ_2 is $R_{\phi_1\phi_2}(r)$ and the one-dimensional spectral density function $E_{\phi_1\phi_2}(k)$ twice its Fourier transform where $k = 2\pi/r$. The spectra are here evaluated in each horizontal computational plane along ξ direction and averaged through η, so that $E = E(\zeta, t, k)$. The integral turbulent scale is $l_L = \pi E(0)/[2R(0)]$ ([31]).

We shall refer to $\boldsymbol{u'} + \tilde{\boldsymbol{u}}$ as the fluctuation field obtained through the usual Reynolds decomposition, where the turbulent field is $\boldsymbol{u'}$ obtained after the filter defined by equations 3 or 4. The spectra are obtained in the final time steps (Red dashed line in figure 1a) and first exemplified in figure 3a by the fluctuations' kinetic energy spectral density functions evaluated in different horizontal planes. The wave

signature is evident in the fluctuations' spectra, leading to the peaks occurring in the swell free (k_w) and bounded (nk_w, $n = 2..5$) wave numbers. As expected the peaks are damped with height but the principal mode is still disturbed for mean heights above 20 m. The theoretical slope is generally recovered below the integral scales (Vertical lines) in the spectra presented in figure 3.

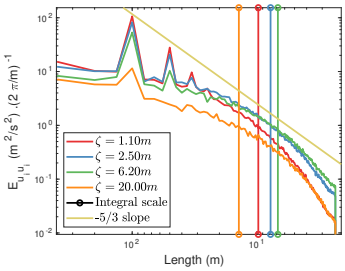

(a) $(u_i'u_i')$ SDF; wavy BC without wave related filters.

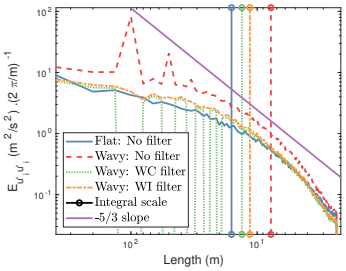

(b) $(u_i'u_i')$ SDF; ζ=2.5 m.

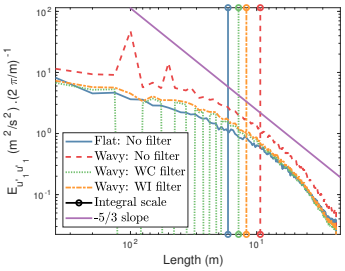

(c) $(u'u')$ SDF; ζ=2.5 m.

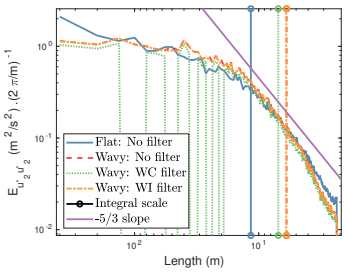

(d) $(v'v')$ SDF; ζ=2.5 m.

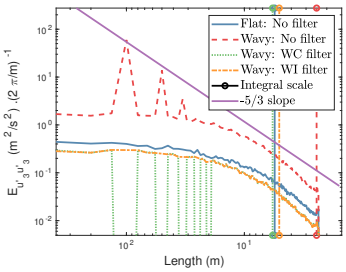

(e) $(w'w')$ SDF; ζ=2.5 m.

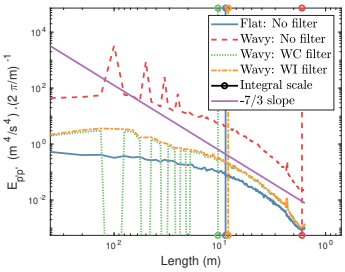

(f) $(p'p')$ SDF; ζ=2.5 m.

Figure 3: Turbulent and fluctuations' spectral density functions (SDF) evaluated in computational planes denoted by their mean physical altitude $\zeta = \overline{x}^{[\xi,\eta]}$.

The turbulent spectra obtained with the filters proposed by equations 3 (WC filter) and 4 (WI filter) are superposed to the fluctuations' spectra (No filter) in figure 3b. As mentioned the turbulent spectra obtained with eq. 3 are completely depleted of its energy in the filtered scales, which is corrected by eq. 4 leading to a close resemblance to the flat bottom case. The integral scale is diminished by the wave's introduction. Most of the integral scale change is due to filtered wave induced motions, but some persist in the spectra after the filtering. The integral scale predicted after the WI filter is between the ones from 'No filter' or 'WC filter' cases. The smaller turbulent scales result from wave induced and turbulent motions interactions: Both vorticity fields occur in the same sense, so that in the encounter of two coherent vorticity structures, streamlines collide with opposing momentum and vortices breakdowns are induced (c.f. [32]).

The proposed modulated filter is further explored in comparison to the reference flat bottom case between figures 3c and 3f through turbulent and fluctuations', velocity components and pressure auto-correlation spectral density functions. The longitudinal velocity spectra are comparable to the turbulent kinetic energy ones already discussed. The transversal velocities spectra present negligible wave induced signature. The higher disturbances are observed in vertical velocity and pressure turbulent spectra: After the wave induced filtering those spectra are approximated to the non-disturbed reference, mostly reproducing its shape but not its intensity.

The obtained squared root of the wave induced energy fraction $f_{ki}(z)$ is averaged over one hour with a reduced time sampling if compared to section 2.1 and shown in figure 4 for each of the decomposed fields and wave numbers. The decay with height is better noted in longitudinal and vertical velocities where f smoothly decays from $f \sim 1$ up to $f \sim 0$ at $z \sim 60m$. No wave induced flow is observed for transversal velocities, so that its energy fraction is composed by noise only and thus not shown for the sake of brevity. As pressure propagates with infinity speed in incompressible flows, the wave induced pressure rapidly reaches the top of the domain not being properly damped above the WBL. As a result wave induced flow dominate pressure fluctuations up until the domain's vertical extension. The wave induced pressure oscilations on the upper surface are a non-desired but well known problem in high

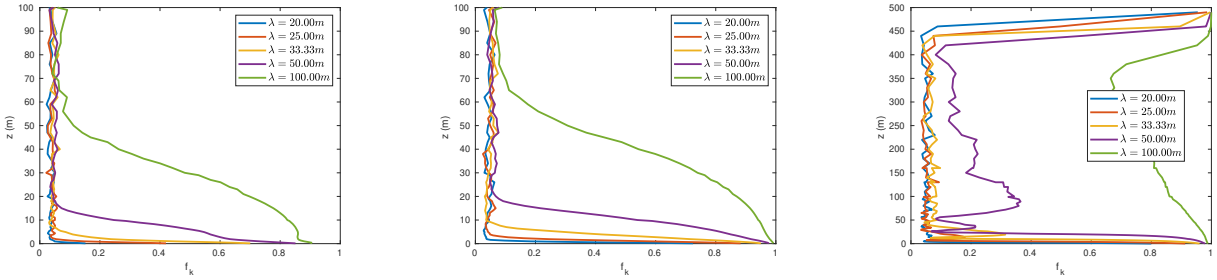

(a) $f_{\lambda_k}(z)$ for u velocity field. (b) $f_{\lambda_k}(z)$ for w velocity field. (c) $f_{\lambda_k}(z)$ for pressure field.

Figure 4: squared root of the wave induced energy fraction $\boldsymbol{f}_{\lambda_k}(z)$, defined in equation 4.

resolution CFD incompressible applications that involve oscilatory moving lower boundaries ([1]). The decay in f_k is more rapid for lower wave numbers, but it is still unclear how much this is due to weaker BC's wave forcing or the fluctuations' behavior in those specific scales.

3 Conclusion

A canonical test case is presented where a reasonably sized swell ($ka = 0.2$, $\lambda = 100$ m), described by 5th order theoretical solution, meets light wind conditions. It is shown that turbulent quantities might be disturbed at heights way above the WBL and into the exploitation zone of current offshore wind turbines such as the FLOATGEN (Le Croisic, France). A wave induced flow definition is proposed which considers its correlation with turbulence, thus allowing further investigation of the coupled dynamics between those fields. The decomposition must rely on turbulent and wave induced physical characteristics to define the non-linear physical parameters $\boldsymbol{f}$, which are here obtained to recover turbulent spectral density functions' shapes as expected from classical flat terrain turbulent motions. This particular strategy is suitable for regular seas but should be adapted otherwise, possibly considering space-time spectra instead of space only. The wave induced filter proposed recover the expected turbulent behavior, though turbulent scales are distorted and particularly the integral scale is consistently diminished. The wave induced and turbulent correlations explain how wave induced effects merge into the turbulent cascade distorting and forcing the turbulent flow above the WBL. A natural definition of the WBL height that require negligible ($< 1\%$) wave induced energy compared to the total energy in a given wave number occurs when $f < 0.1$: Leading to a WBL height of $\sim 0.5\lambda$ or $\sim 0.7\lambda$ if longitudinal or vertical motions are respectively considered.

References

[1] M. Cathelain, *Development of a deterministic numerical model for the study of the coupling between an atmospheric flow and a sea state*. PhD thesis, Ecole Centrale de Nantes (ECN), 2017.

[2] P. P. Sullivan, J. C. McWilliams, and E. G. Patton, "Large-eddy simulation of marine atmospheric boundary layers above a spectrum of moving waves," *Journal of the Atmospheric Sciences*, vol. 71, no. 11, pp. 4001–4027, 2014.

[3] G. Ducrozet, F. Bonnefoy, D. L. Touz, and P. Ferrant, "Hos-ocean: Open-source solver for nonlinear waves in open ocean based on high-order spectral method," *Computer Physics Communications*, vol. 203, pp. 245–254, 2016.

[4] T. Foken, "50 years of the monin–obukhov similarity theory," *Boundary-Layer Meteorology*, vol. 119, no. 3, pp. 431–447, 2006.

[5] H. Tamura, W. Drennan, C. Collins, and H. Graber, "Turbulent airflow and wave-induced stress over the ocean," *Boundary-Layer Meteorology*, pp. 1–20, 2018.

[6] T. Hristov, "Mechanistic, empirical and numerical perspectives on wind-waves interaction," *Procedia IUTAM*, vol. 26, pp. 102–111, 2018.

[7] J. D. Fenton, "A fifth-order stokes theory for steady waves," *Journal of waterway, port, coastal, and ocean engineering*, vol. 111, no. 2, pp. 216–234, 1985.

[8] W. Thomson, "Hydrokinetic solutions and observations," *Philosophical Magazine*, vol. 42, pp. 326–378, 1871.

[9] H. Jeffreys, "On the formation of water waves by wind," in *Procceedings of the Royal Society of London* (T. R. Society, ed.), vol. 107, pp. 189–206, 1925.

[10] O. M. Philips, "On the generation of waves by turbulent wind," *Journal of Fluid Mechanics*, vol. 2, pp. 417–445, 1957.

[11] J. W. Miles, "On the generation of surface waves by shear flows, parti," *Journal of Fluid Mechanics*, vol. 3, pp. 185–204, 1957.

[12] J. W. Miles, "On the generation of surface waves by shear flows, partii," *Journal of Fluid Mechanics*, vol. 6, pp. 568–582, 1959.

[13] M. J. Lighthill, "Physical interpretation of the mathematical theory of wave generation by wind," *Journal of Fluid Mechanics*, vol. 14, pp. 385–398, 1962.

[14] S. E. Belcher and J. C. R. Hunt, "Turbulent shear flow over slowly moving waves," *Journal of Fluid Mechanics*, vol. 251, pp. 109–148, 1993.

[15] E. G. Patton, P. P. Sullivan, B. Kosovi, J. Dudhia, L. Mahrt, M. agar, and T. Mari, "On the influence of swell propagation angle on surface drag," *Journal of Applied Meteorology and Climatology*, vol. 58, no. 5, pp. 1039–1059, 2019.

[16] S. Porchetta, O. Temel, D. Muñoz Esparza, J. Reuder, J. Monbaliu, J. van Beeck, and N. van Lipzig, "A new roughness length parameterization accounting for wind–wave (mis)alignment," *Atmospheric Chemistry and Physics*, vol. 19, no. 10, pp. 6681–6700, 2019.

[17] J. B. Edson, V. Jampana, R. A. Weller, S. P. Bigorre, A. J. Plueddemann, C. W. Fairall, S. D. Miller, L. Mahrt, D. Vickers, and H. Hersbach, "On the exchange of momentum over the open ocean," *Journal of Physical Oceanography*, vol. 43, no. 8, pp. 1589–1610, 2013.

[18] P. A. E. M. Janssen, Ø. Breivik, K. Mogensen, F. Vitart, M. Alonso-Balmaseda, J.-R. Bidlot, S. Keeley, M. Leutbecher, L. Magnusson, and F. Molteni, "Air-sea interaction and surface waves," *ECMWF Technical Memorandum*, 2013.

[19] H. Charnock, "Wind stress on a water surface," *Quarterly Journal of the Royal Meteorological Society*, vol. 81, pp. 639–640, 10 1955.

[20] M. A. Donelan, F. W. Dobson, S. D. Smith, and R. J. Anderson, "On the dependence of sea surface roughness on wave development," *Journal of Physical Oceanography*, vol. 23, no. 9, pp. 2143–2149, 1993.

[21] J. P. OSullivan, R. Archer, and R. G. J. Flay, "Consistent boundary conditions for flows within the atmospheric boundary layer," 2011.

[22] B. Blocken, "50 years of computational wind engineering : past, present and future," *Journal of Wind Engineering and Industrial Aerodynamics*, vol. 129, pp. 69–102, 2014.

[23] P. P. SULLIVAN, J. C. McWILLIAMS, and C.-H. MOENG, "Simulation of turbulent flow over idealized water waves," *Journal of Fluid Mechanics*, vol. 404, p. 4785, 2000.

[24] P. P. Sullivan, J. B. Edson, T. Hristov, and J. C. McWilliams, "Large-eddy simulations and observations of atmospheric marine boundary layers above nonequilibrium surface waves," *Journal of the Atmospheric Sciences*, vol. 65, no. 4, pp. 1225–1245, 2008.

[25] C.-H. Moeng, M. A. LeMone, M. F. Khairoutdinov, S. K. Krueger, P. A. Bogenschutz, and D. A. Randall, "The tropical marine boundary layer under a deep convection system: a large-eddy simulation study," *Journal of Advances in Modeling Earth Systems*, vol. 1, no. 4, 2009.

[26] "Effect of downwind swells on offshore wind energy harvesting a large-eddy simulation study," *Renewable Energy*, vol. 70, pp. 11 – 23, 2014. Special issue on aerodynamics of offshore wind energy systems and wakes.

[27] E. A. Spiegel and G. Veronis, "On the boussinesq approximation for a compressible fluid," *Astrophysical Journal, vol. 131, p.442*, 1960.

[28] T. Hristov and J. Ruiz-Plancarte, "Dynamic balances in a wavy boundary layer," *Journal of Physical Oceanography*, vol. 44, no. 12, pp. 3185–3194, 2014.

[29] A. Cifuentes-Lorenzen, J. B. Edson, and C. J. Zappa, "Airsea interaction in the southern ocean: Exploring the height of the wave boundary layer at the airsea interface," *Boundary-Layer Meteorology*, vol. 169, pp. 461–482, 2018.

[30] X. Hao and L. Shen, "Windwave coupling study using les of wind and phase-resolved simulation of nonlinear waves," *Journal of Fluid Mechanics*, vol. 874, p. 391425, 2019.

[31] S. B. Pope, *Turbulent Flows*. Cambridge University Press, 2000.

[32] H. K. Moffatt and A. Tsinober, "Helicity in laminar and turbulent flow," *Annual Review of Fluid Mechanics*, vol. 24, no. 1, pp. 281–312, 1992.